

SUPPORTING INFORMATION

Bi-functional Interfaces by Poly-Ionic Liquid Treatment in Efficient *pin* and *nip* Perovskite Solar Cells

Pietro Caprioglio^{a,b*}, Daniel Saul Cruz^c, Sebastián Caicedo-Dávila^d, Fengshuo Zu^e, Albertus Adrian Sutanto^f, Francisco Peña-Camargo^a, Lukas Kegelmann^b, Daniele Meggiolaro^m, Luca Gregoriⁿ, Christian M. Wolff^a, Burkhard Stiller^a, Lorena Perdigón-Toro^a, Hans Kobler^l, Bor Li^b, Emilio Gutierrez-Partida^a, Iver Lauermann^d, Antonio Abate^l, Norbert Koch^e, Filippo De Angelis^{m,n,o}, Bernd Rech^g, Giulia Grancini^{f,i}, Daniel Abou-Ras^d, Mohammad Khaja Nazeeruddin^f, Martin Stoltterfoht^a, Steve Albrecht^{b,h}, Markus Antonietti^c and Dieter Neher^{a*}

^a Institute of Physics and Astronomy, University of Potsdam, 14476 Potsdam, Germany

^b Young Investigator Group Perovskite Tandem Solar Cells, Helmholtz-Zentrum Berlin für Materialien und Energie GmbH, 12489 Berlin, Germany

^c Max Planck Institute of Colloids and Interfaces, Am Mühlenberg 1, 14476 Potsdam, Germany

^d Helmholtz Zentrum Berlin für Materialien und Energie GmbH, 12489 Berlin, Germany

^e Humboldt University, Institut für Physik, Newtonstraße 15, 12489 Berlin, Germany

^f Group for Molecular Engineering of Functional Materials, Institute of Chemical Sciences and Engineering, École Polytechnique Fédérale de Lausanne, CH-1951 Sion, Switzerland

^g Institute for Silicon Photovoltaics, Helmholtz-Zentrum Berlin für Materialien und Energie GmbH, 12489 Berlin, Germany

^h Faculty IV – Electrical Engineering and Computer Science Technical, University Berlin, 10587 Berlin, Germany

ⁱ Department of Chemistry, University of Pavia, Via Torquato Taramelli 14, 27100 Pavia, Italy

^l Young Investigator Group Active Materials and interfaces for stable perovskite solar cells

Helmholtz-Zentrum Berlin für Materialien und Energie GmbH, 12489 Berlin, Germany

^m Computational Laboratory for Hybrid/Organic Photovoltaics (CLHYO), Istituto CNR di Scienze e Tecnologie Chimiche “Giulio Natta” (CNR-SCITEC), Via Elce di Sotto 8, 06123 Perugia, Italy

ⁿ Department of Chemistry, Biology and Biotechnology, University of Perugia, Perugia, Italy

^o CompuNet, Istituto Italiano di Tecnologia, Via Morego 30, 16163 Genova, Italy

Corresponding author: neher@uni-potsdam.de, capriogl@uni-potsdam.de

S1: PILs Characterization

The average molecular weight of the PIL is found to be 130kDa as reported from by gel permeation chromatography.¹

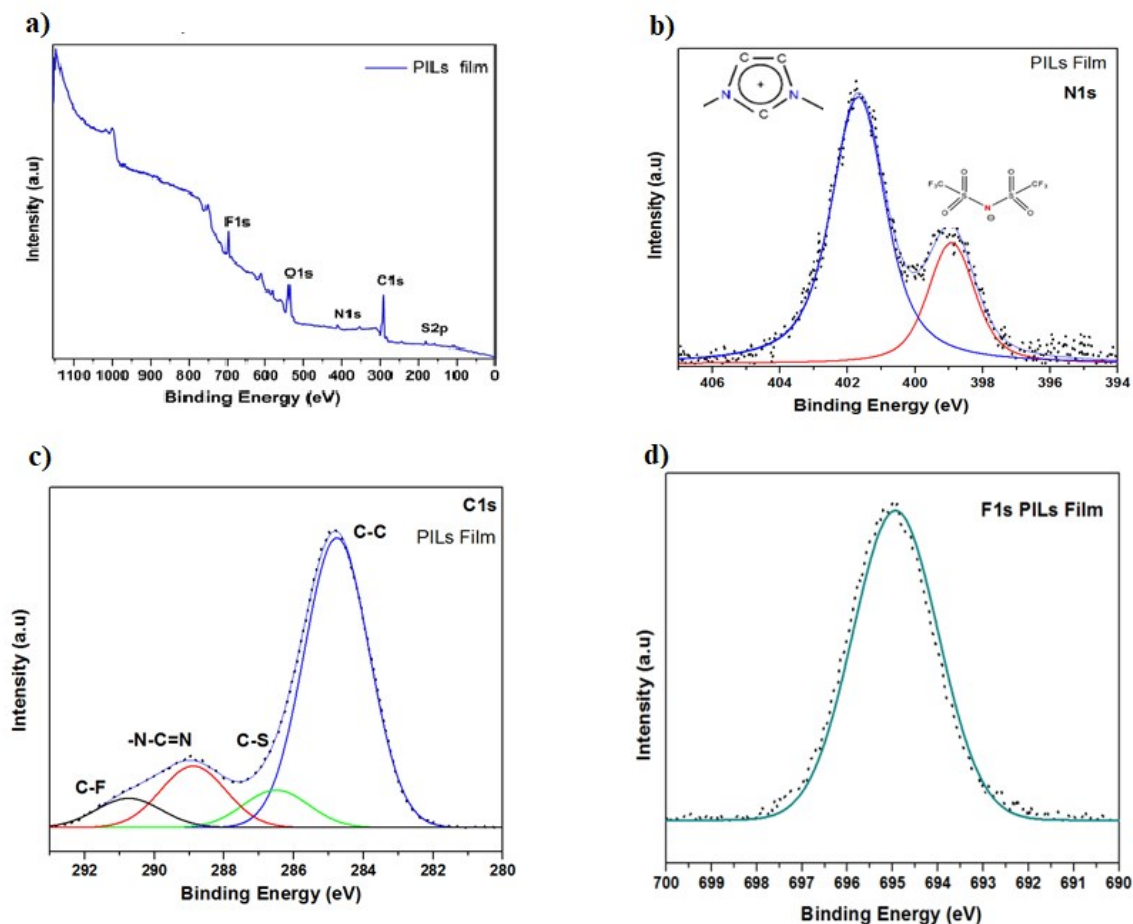


Fig. S1A: X-ray Photoelectron Spectroscopy (XPS) from [PeIm][TFSI] spray-coating thin films with MgK α like excitation source, **a)** XPS survey spectrum, **b)** High resolution XPS of C1s spectrum core level **c)** High resolution XPS of N1s spectrum core level **d)** High resolution XPS of F1s spectrum core level

Table S1: Solubility of PILs([PeIm][TFSI]) in several solvents at room temperature

Solvent	Soluble	Insoluble
Toluene		X
Acetonitrile	X	
Dichloromethane	X	
Methanol		X
Water		X
Acetone		X
2-propanol		X

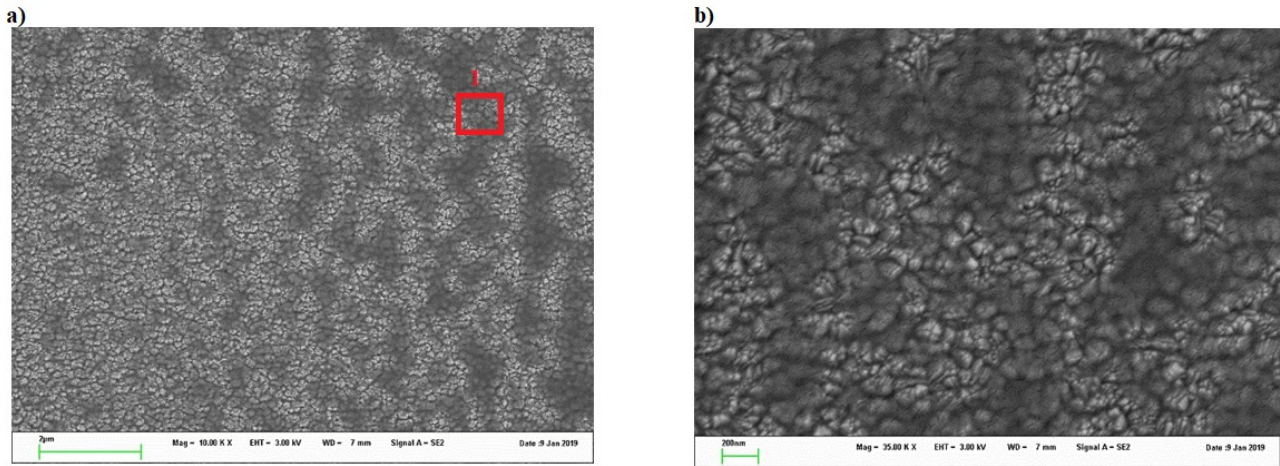
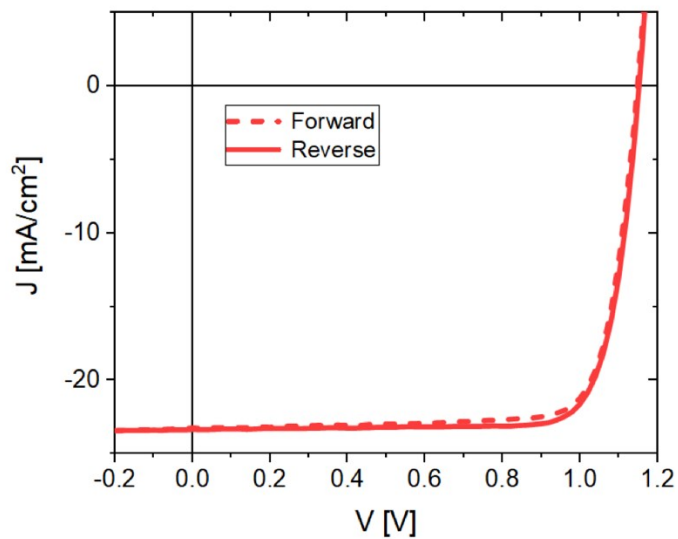


Fig. S1B: Scanning electron microscopy images of the top surface of the [PeIm][TFSI] thin film **a)** Magnification of 10KX and **b)** Magnification of SEM from the region 1.

S2: Additional J-V



	V_{oc} [V]	J_{sc} [mA/cm ²]	FF [%]	PCE [%]
Fw	1.148	22.7	79.8	20.8
Rv	1.152	22.8	79.2	20.8

Figure S2A: Forward and reverse J-V scans (0.02 V/s with a voltage step of 0.02 V) for a PIL treated solar cell. There is very little hysteresis, particularly in the important voltage range near V_{oc} .

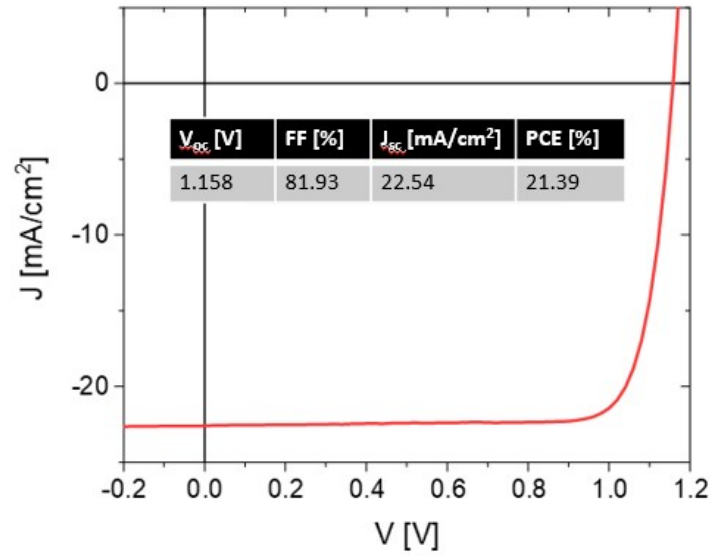


Figure S2B: Reverse J - V scans (0.02 V/s with a voltage step of 0.02 V) for the champion PIL treated solar cell measured with a mask.

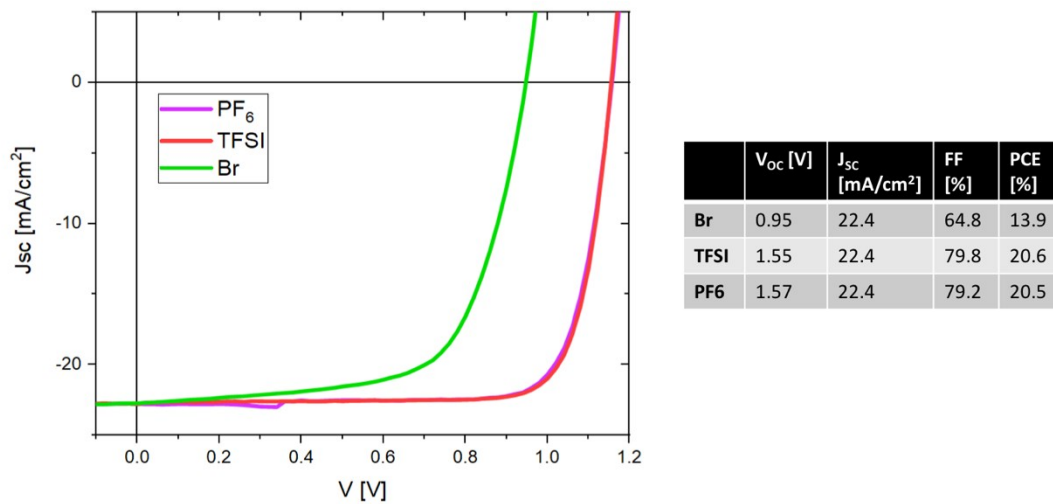


Fig. S2C: J - V scans of perovskite solar cells treated with different PILs: $[PeIm][TFSI]$, $[PeIm][Br]$ and $[PeIm][PF_6]$. While the TFSI and PF_6 version demonstrate a very similar performance, the Br version decreases the efficiency significantly.

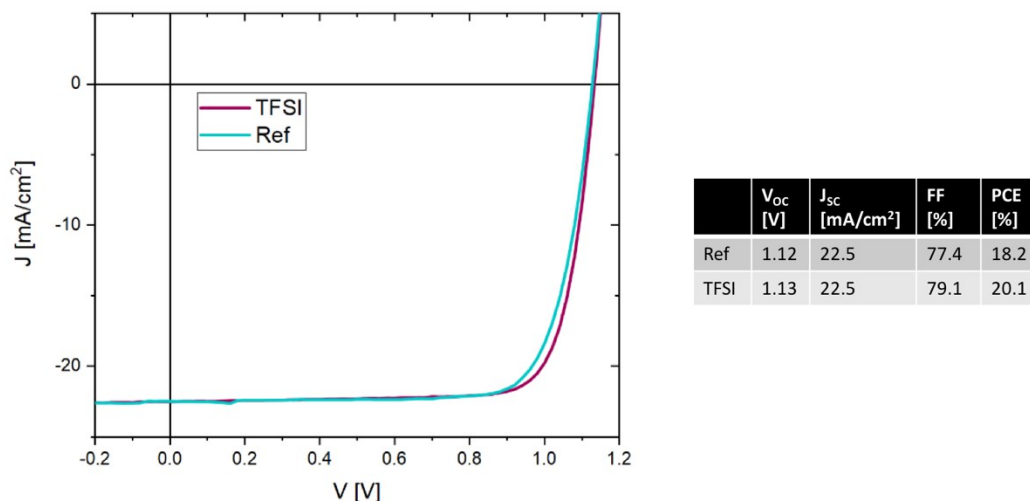


Fig. S2D: *JV scans for perovskite solar cells with and without Li-TFSI interlayer. Here, the addition of LiTFSI increase the FF of 2% absolute.*

S3: EQE_{PV} - Absorption

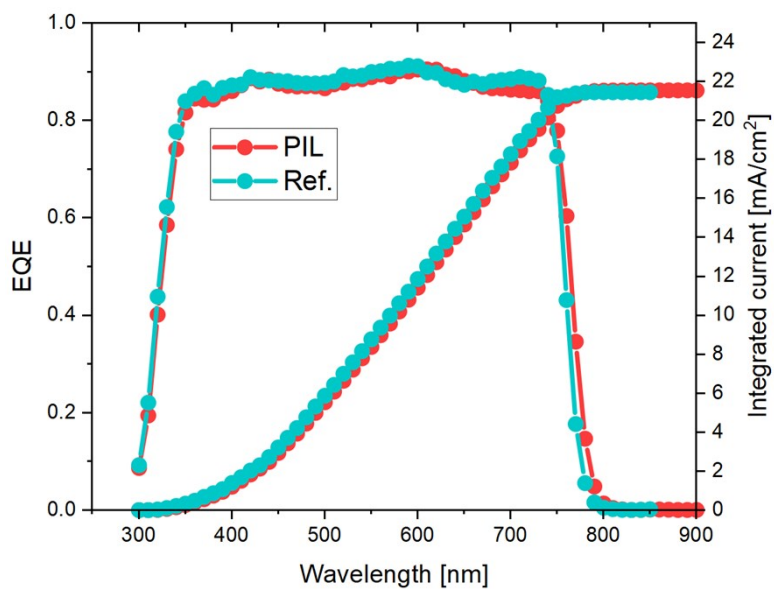


Figure S3A: *External Quantum Efficiency including the integrated current for reference and PIL treated cells. We note that the EQE on the PIL sample shows a very small red-shift. However, given the fact that we didn't observe any change in PL emission, absorption or J_{SC} , we attribute that to a simple batch to batch variation. Importantly, since such an effect has not manifested in any other experiment or been found to be impactful in any other measurements, we disregarded the possibility to have a bandgap change upon PIL surface modification.*

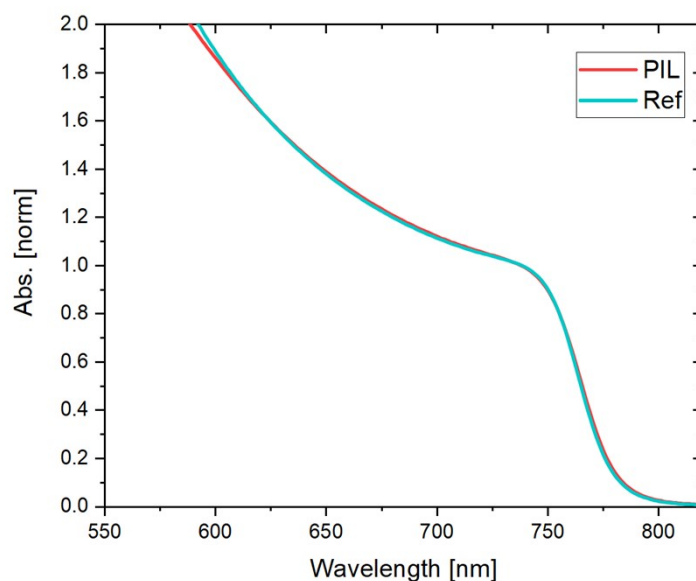


Figure S3B: Absorbance of the reference and PIL treated perovskite films.

S4: DFT report: PIL-TFSI passivation of LHP

The adsorption of [PeIm] and [TFSI] molecules on the (001) surface of MAPbI_3 is investigated by means of density functional theory methods by using the PBE functional.² PIL polymer has been modelled by considering a single monomer terminated by CH_3 units.

Starting from the half MAI-terminated surface, i.e. MAI (50%), MAI units have been replaced by PIL-TFSI units to form MAI(25%)@[PeIm][TFSI](25%) and [PeIm][TFSI](50%) surfaces. The thermodynamics of [PeIm][TFSI] adsorption and the effects on the electronic properties of the MAPI surface have been monitored (see Table S4). In the MAI(25%)@[PeIm][TFSI] (25%) surface TFSI nitrogen strongly binds Pb at the surface at distance of 2.8-2.9 Å (see Figure 4A). By increasing [PeIm][TFSI] coverage up to 50% the steric interaction between molecules weakens the Pb-N bond, that increases to 3.2-3.3 Å. The adsorption thermodynamics is analyzed by calculating the adsorption energy of [PeIm][TFSI] and MAI units on the PbI_2 terminated bare surface, results are reported in Table S4. In all cases the passivation of the PbI_2 -terminated surface by MAI or [PeIm][TFSI] molecules is a favored process. The favorable passivation of PbI_2 surface by MAI units is in agreement with the higher stability of MAI-terminated surface with respect to PbI_2 -terminated surface, reported in previous computational works.³

The substitution of 25% of MAI units by [PeIm][TFSI] is slightly disfavored by 0.07 eV / molecule, while the full replacement of MAI with [PeIm][TFSI] is highly disfavored by ~0.5 eV / molecule. The unfavorable energetics of MAI substitution highlights that [PeIm][TFSI] mainly acts as a passivating agent in MAI-poor portions of the perovskite, where TFSI anion strongly binds Pb, stabilizing the surface. The replacement of MAI with [PeIm][TFSI] leads to a small narrowing of the band gap, whose value decreases from 1.82 to 1.77 eV, while an upshift in energy of the VBM is reported by increasing the [PeIm][TFSI] coverage. This is signalled by the decrease of the work function (WF), here calculated as the difference between the vacuum level and the VBM. The increase of the VBM by [PeIm][TFSI] passivation is in agreement with the trend found experimentally.

Table S4. Calculated adsorption energy (E_{ads}), energy gap (E_g), work function (WF), and DFE of iodine Frenkel defect of bare PbI_2 -terminated and passivated $MAPbI_3$ (001) surfaces (PBE level). Asterisks denote DFE of Frenkel defects with I_i bonded to Pb sites not passivated by TFSI. In parenthesis values calculated with the hybrid PBE0 functional at the PBE optimized geometries are reported.

Surface	E_{ads} (eV)	E_{gap} (eV)	WF (eV)	DFE Frenkel (eV)
PbI_2 terminated - MAI (0%)	-	1.53	5.84	-0.05
MAI (50%)	-1.98	1.82	5.29	0.21 (0.18) 0.09*
MAI(25%)@[PeIm][TFSI](25%)	-1.91	1.78	5.22	0.65 0.34*
[PeIm][TFSI] (50%)	-1.47	1.77	4.55	0.76 (0.69)

In order to investigate the effects of [PeIm][TFSI] adsorption on defect equilibria, the energy of formation (DFE) of iodine Frenkel defect, i.e. $V_I^+ + I_i^-$, at the pristine and passivated surfaces is calculated (see Figure 4Ad-f). Iodine interstitial is responsible of the increased non-radiative recombination at the surface and in bulk material.⁴ For [PeIm][TFSI] passivated surfaces Frenkel iodide interstitial has been modelled on TFSI-passivated Pb ions. In the case of MAI(25%)@[PeIm][TFSI] (25%) surface Frenkel iodine interstitial has been modelled on both TFSI-passivated and un-passivated Pb ions at the surface. Results are reported in Table S4.

As reported in Table S4, the DFE of the Frenkel defect on the MAI(25%)@[PeIm][TFSI] (25%) and [PeIm][TFSI] (50%) surfaces is increased compared to the MAI-half terminated (MAI 50%) surface by 0.44 and 0.55 eV, respectively. Notably, the formation of Frenkel defect on the less stable PbI_2 -terminated surface is slightly favored, highlighting that such surface is extremely disordered. This trend is also observed for Frenkel defects with interstitials coordinated by Pb ions not directly passivated by TFSI ion (values with asterisks in Table S4), where a DFE increase of 0.24 eV is calculated.

Furthermore, DFEs of Frenkel defects on the MAI(50%) and [PeIm][TFSI](50%) surfaces have been refined at higher level of theory by performing hybrid functional PBE0⁵ single point calculations at the PBE relaxed geometries. At this level of theory, a DFE difference of 0.51 eV is calculated, in good agreement with PBE results.

The increase in the formation energy of Frenkel defects on the MAI(25%)@[PeIm][TFSI](25%) and [PeIm][TFSI] (50%) surfaces is mainly ascribed to the steric interactions between the [PeIm][TFSI] layer and the iodide interstitial at the interface. In Figure 4B the structural details of the adsorbed TFSI anion on the pristine surface and in the surfaces containing Frenkel defects are reported, along with the optimized Pb-N bond distances. In the case of Frenkel defective slabs iodine interstitials directly bonded to TFSI-passivated Pb ions are reported. Over-coordination of surface Pb by interstitial iodide leads to the weakening of the Pb-N bond (Pb-N bond lengths > 4 Å) with an overall destabilization of the surface and a consequent increase of the DFE. This is observed also for Frenkel defects on the MAI(25%)@[PeIm][TFSI](25%) with I_i not directly bonded to TFSI-passivated Pb ions, where an increase of the Pb-N distance from 2.8-2.9 Å to 3.1-3.3 Å is reported.

Overall, these results suggest that [PeIm][TFSI] treatment may potentially decrease the density of Frenkel defects by passivating Pb surface ions in MAI-poor portions of the perovskite, thus reducing non-radiative recombination.

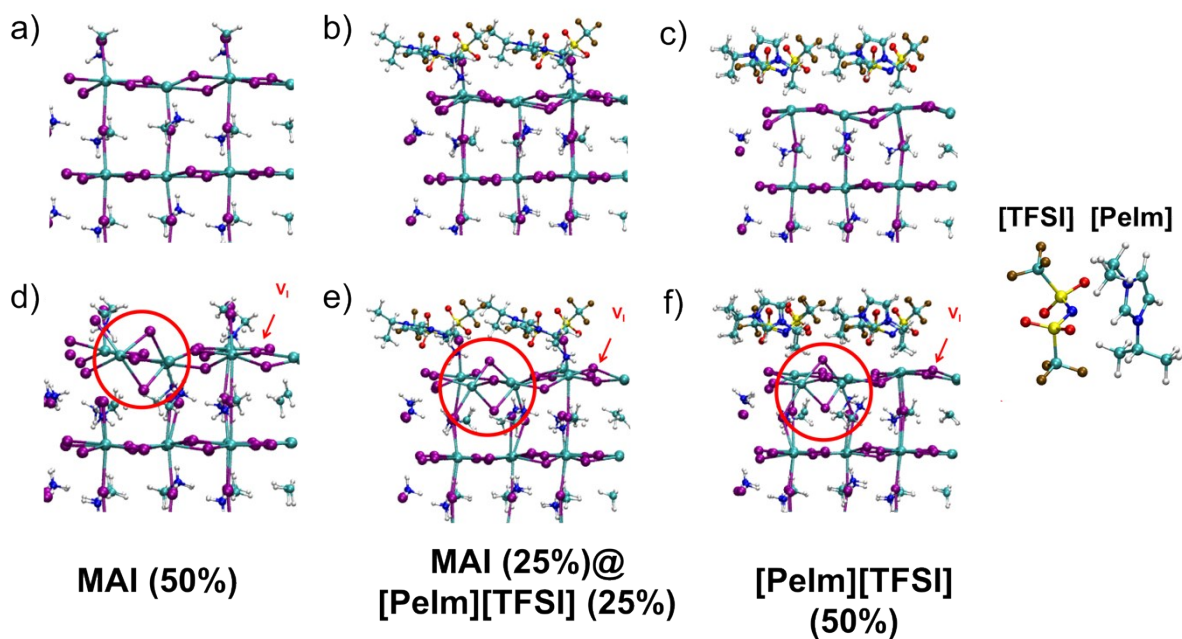


Figure 4A. Structure of a) MAI-half terminated (MAI 50%) surface; b) MAI(25%)@[PeIm][TFSI](25%); c) [PeIm][TFSI] (50%) surface; d-f) the same surfaces in presence of a Frenkel defect.

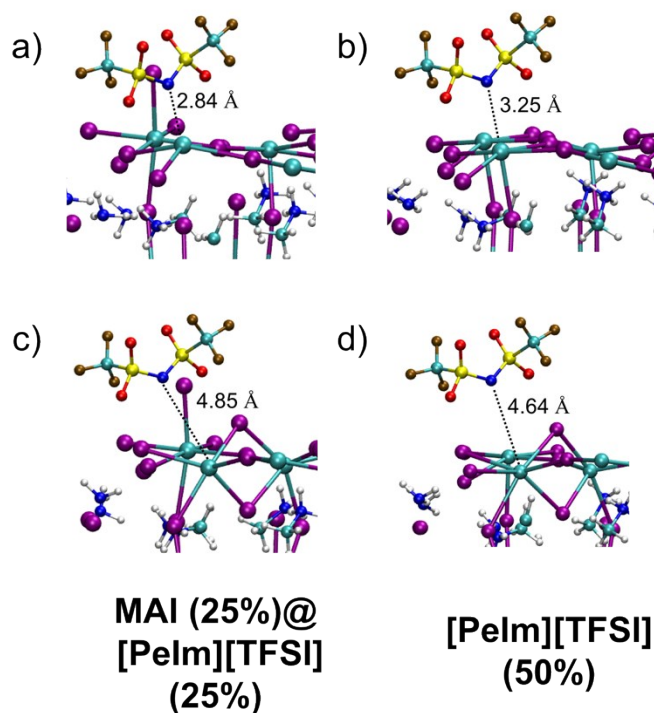


Figure 4B. Structural detail of the TFSI anion adsorbed on a) pristine MAI(25%)@[PeIm][TFSI](25%) surface; b) pristine [PeIm][TFSI] (50%) surface; c) MAI(25%)@[PeIm][TFSI] (25%) surface with a Frenkel defect; d) [PeIm][TFSI] (50%) surface with Frenkel defect. For clarity, only the TFSI ion adsorbing on the over-coordinated Pb is reported, while all other molecules at the surface have been omitted.

Computational details

DFT calculations have been performed by using the CP2K software package.⁶ DZVP gaussian basis set⁷ and Goedecker-Teter-Hutter pseudopotentials⁸ have been used along with the PBE functional² and DFTD3 dispersion corrections⁹. A charge density cutoff of 500 Ry was used throughout calculations.

Hybrid functional single point calculations have been performed by using the same computational setup described above and by using the PBE0 functional, by keeping the exact exchange fraction to the default $\alpha=0.25$ value. The auxiliary density matrix method¹⁰ has been used in order to accelerate hybrid functional calculations.

2x2 in-plane surface slabs with five PbI layers were used in calculations within the supercell approach, by fixing cell parameters to the experimental values,¹¹ and introducing in all cases a vacuum layer > 10 Å in the direction perpendicular to the slab.

Adsorption energies of MAI and PIL-TFSI molecules on the PbI₂ terminated surface have been calculated by using energies of neutral MAI and PIL-TFSI clusters modelled in vacuum. Work functions of surfaces have been estimated by subtracting the VBM to the potential in the vacuum region.

S5: X-Ray Diffraction

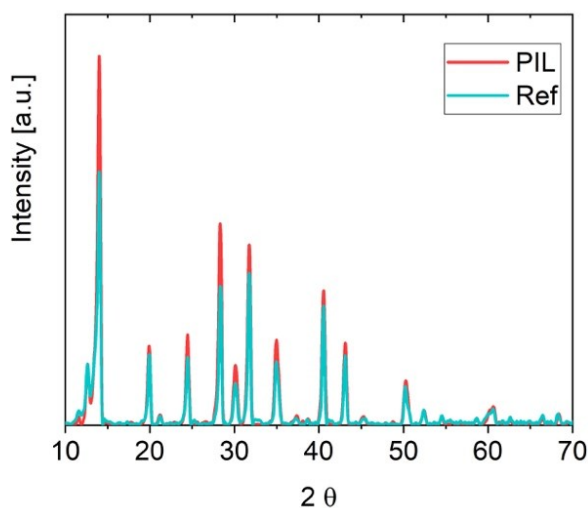


Figure S5: X-ray diffraction for the neat perovskite reference and the PIL treated one. We notice that the PIL treatment do not induce a significant change in the crystallinity of the sample nor induce the appearing of a secondary phase. We note that the slightly lower intensity in the peaks of the reference sample can be simply attributed to a difference in the crystal orientation.

S6: Contact Angle

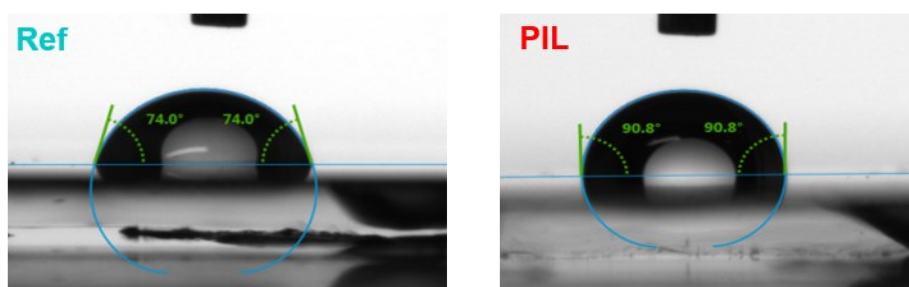


Figure S6: Contact angle measurements using water for a neat reference and a PIL treated perovskite. We note that for the PIL treated sample the contact angle with water is larger, denoting a stronger hydrophobicity of the surface. The effect is expected due to the deposition of a hydrophobic material (PIL) on top of the perovskite surface.

S7: Scanning Electron Microscopy

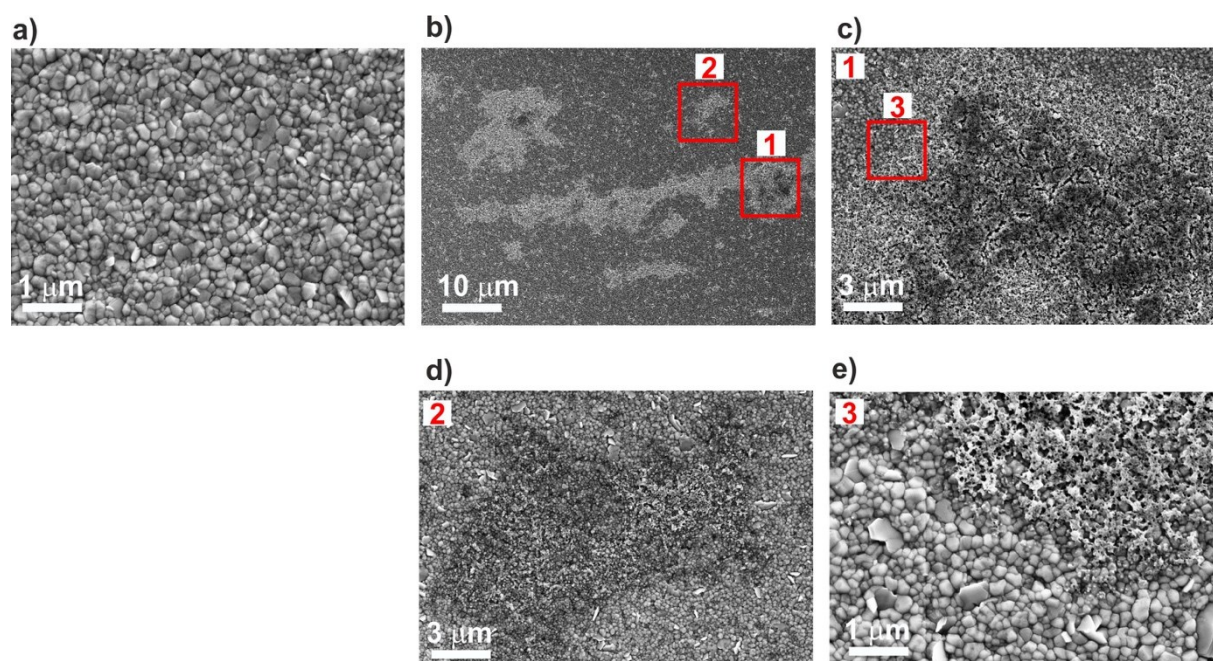


Figure S7A: Scanning electron microscopy images of the top surface of the reference perovskite a) and of the PIL treated surface b)-e). In b) the polymer patches spread around the surface after spin coating. In c) and d) the central spot of this polymer island is magnified and the porous nature of the material is observed. In e) we can identify the border between the underlying perovskite and the polymer, it is evident that the polymer attaches to the perovskite top layer without penetrating in it.

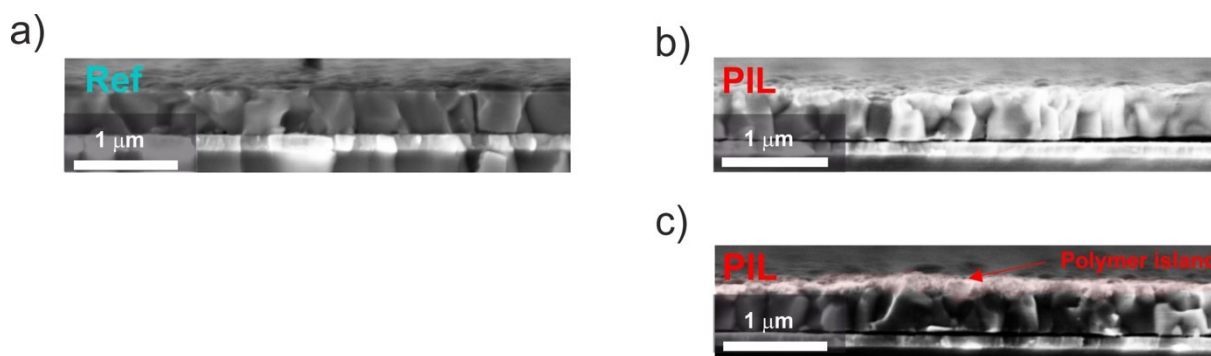


Figure S7B: Cross section SEM images of a reference a) and PIL treated perovskite films b)-c) deposited on ITO/PTAA. In b) the cross section image of the PIL treated perovskite sample is representing an area where there are no polymer highlands present at the surface. In c) the cross section represents an area where the perovskite is covered by a polymer island. Both images do not show any sign of alteration of the bulk structure compared to the reference perovskite nor penetration of the PIL in the bulk.

S8: Additional EDX

Given the low signal of S and the covering of the F signal from the I, much highly concerted, we addressed the O signal as characteristic of the TFSI counterion. Naturally, we checked the reliability of the signal by comparing the treated and neat perovskite in order to verify that the O was coming exclusively from the TFSI and not from the environment, as shown in Fig. 4 in the main text.

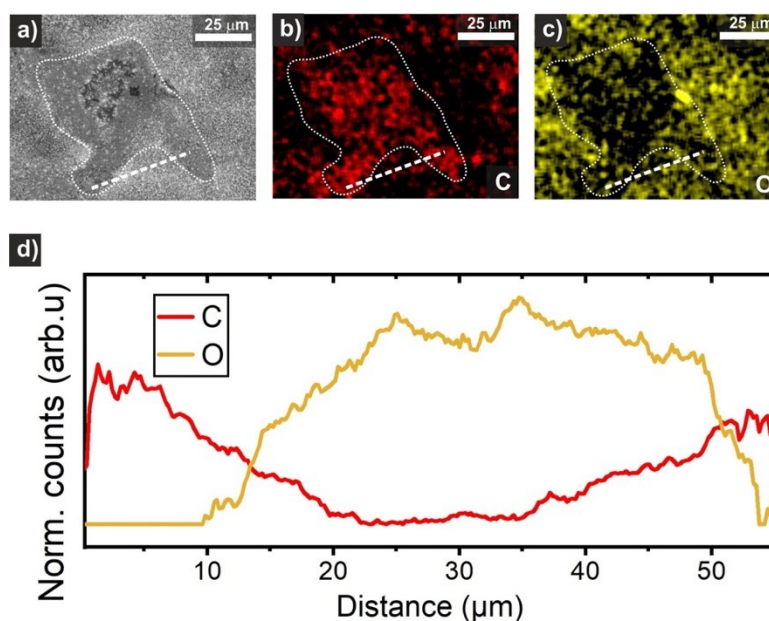


Figure S8A: SEM a) and EDX b)-c) top surface of a PIL treated perovskite. The line scan of the C and O contraction is indicated by the thick white dotted lines and the concentration profile plotted in d). It is clearly visible the anticorrelation between C and O signal at the top surface.

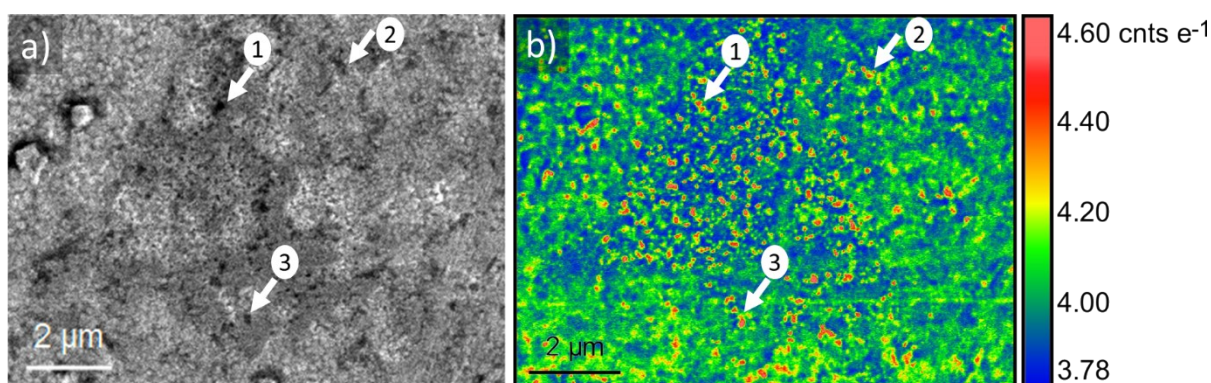


Figure S8B: SEM image (a) and corresponding CL map (b) of an area of the PIL-treated perovskite film covered by a polymer island. Note that the apparent high CL-intensity spots on the polymer island correspond to pores, which indicate that the enhanced luminescence stems from the underlying passivated perovskite, as shown with arrows for the points 1, 2 and 3. The uncovered perovskite still exhibits luminescence enhancement.

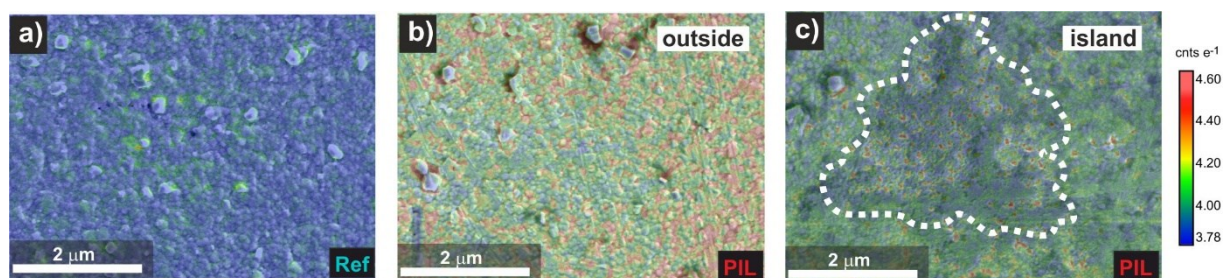


Figure S8C: Superposition of SEM and CL images of the top surface of an untreated perovskite a), a PIL treated perovskite outside the polymeric islands b) and PIL treated perovskite on a polymeric island. Notably, where the reference samples present a certain degree of correlation between topography and CL emission, in the PIL samples the enhanced luminescence seems to be not correlated with the topography. Particularly, the high luminescence passivated spots are invisible on the bare SEM image.

S9: AFM / CAFM

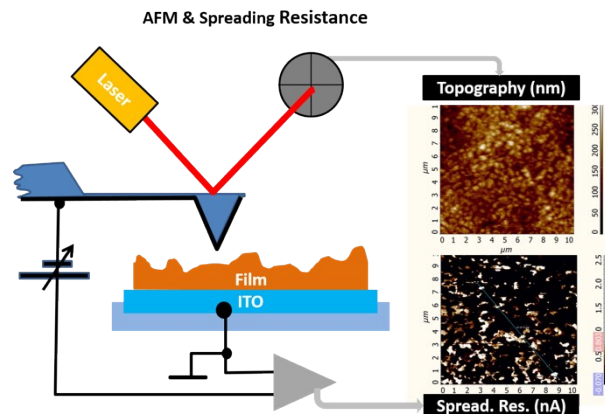


Figure S9A: Schematic representation of the CAFM setup, where a positive or negative bias is applied to the platinum coated tip with regard to the grounded ITO bottom electrode.

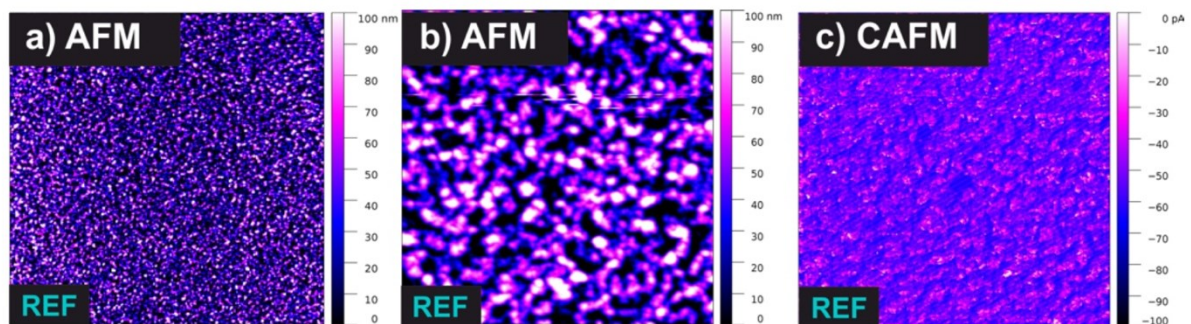


Figure S9B: AFM and CAFM images of the neat reference perovskite. We notice that the top surface presents a rather homogeneous topography on large scale a) of 50x50 μm. In b) and c) AFM and CAFM is directly compared (10x10 μm). The CAFM image shows a homogeneous low current response for the whole surface scanned.

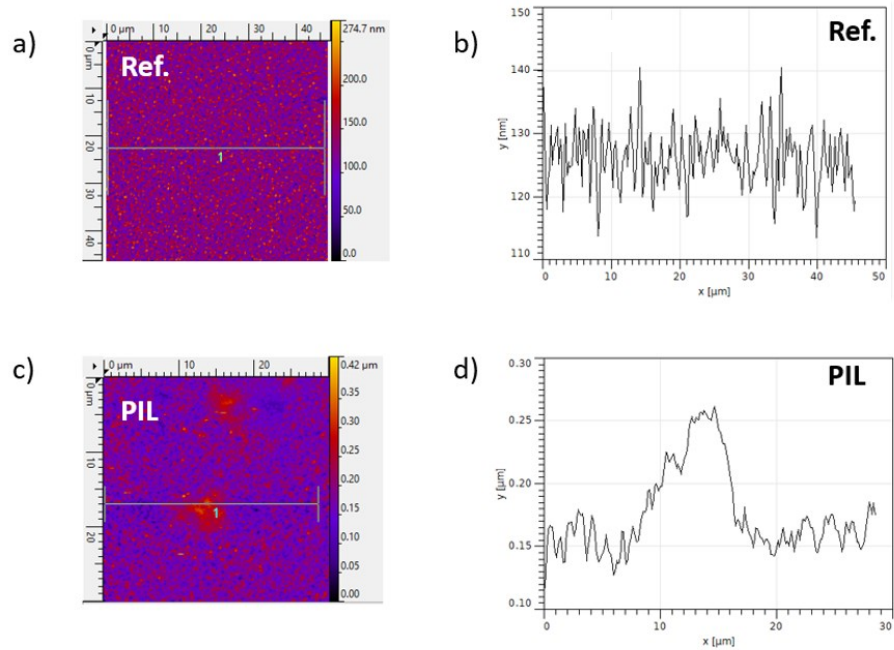
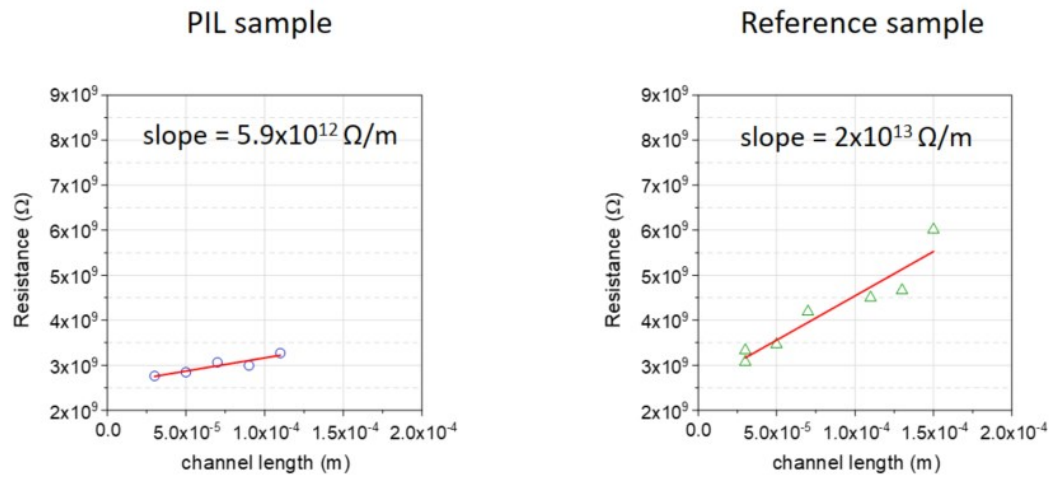


Figure S9C: Topography AFM images of the neat reference perovskite a) and PIL treated one c) with the respective height line scan b) and d). The line scan shows a rather homogenous surface for the reference samples whereas for the PIL treated one, islands as high as 100 nm are visible.

S10: Conductivity



$$R_T = 2R_C + R_S = 2R_C + \frac{\rho l}{wd}$$

$w=1$ cm (from electrode)
 $d=500$ nm

$$\rho = \frac{1}{\sigma}$$

Sample	Conductivity [S/cm]
PIL	$3.6 \times 10^{-7} \pm 0.8 \times 10^{-7}$
Ref	$1.0 \times 10^{-7} \pm 0.2 \times 10^{-7}$

1

Figure S10: Measurement of the lateral conductivity in a two-electrode configuration. By performing these measurements for different electrode distances (channel lengths), the total resistance R_T can be subdivided into the contact resistance (R_C) and the resistance of the sample (R_S). The sample resistance R_S was translated into a lateral sample conductivity by assuming that the full absorber thickness contributes to the current transport. The measurements indicate an increase in conductivity upon PIL addition. The increase of the total resistance is less pronounced with the PIL, which we attribute to a higher lateral conductivity of the PIL-treated sample.

S11: Dark Currents

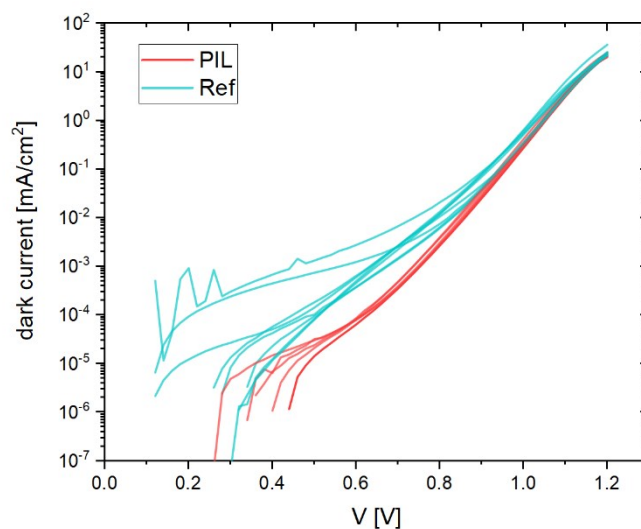


Figure S11: Dark J - V characteristic of the series of devices with and without PIL treatment. For the PIL treated devices the dark J - V show lower leakage currents in the low voltage range compared to the reference samples, suggesting the presence of a better contact.

S12: Photoelectron Spectroscopy

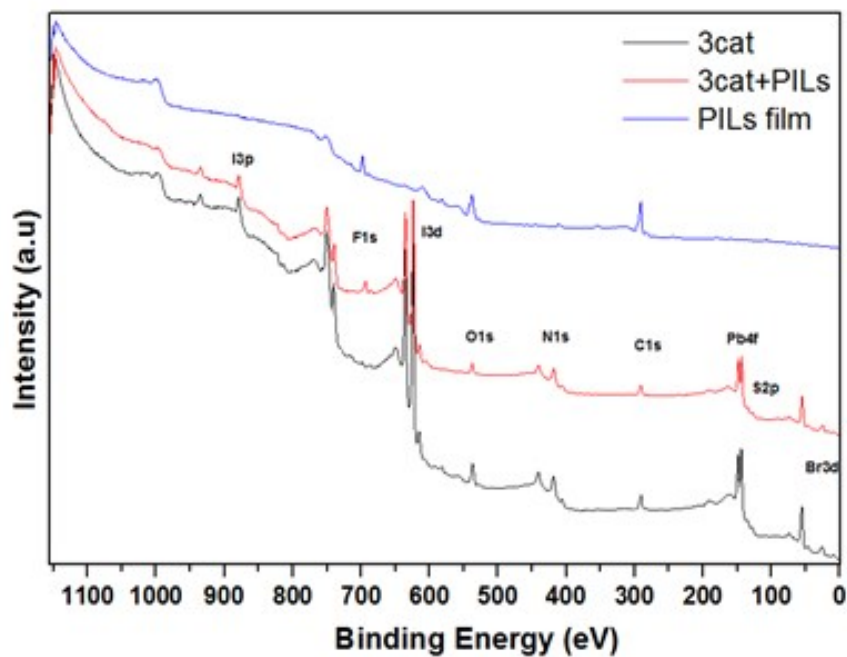


Figure S12A: XPS survey for 3 cat-perovskite, after $[PeIm][TFSI]$ implementation and $[PeIm][TFSI]$ bare thin film. The scans show the characteristic core levels of the elements present in our halide perovskite: $I3p$, $I3d$, $N1s$, $C1s$, $Pb4f$, and $Br3d$. Additionally, on the PIL treated surface, the emerging peaks at 688 eV and 165 eV corresponds to $F1s$ and $S2p$, indicating the polymer adhesion on perovskite surface.

S13: Radiative Limit and quasi-Fermi level splitting

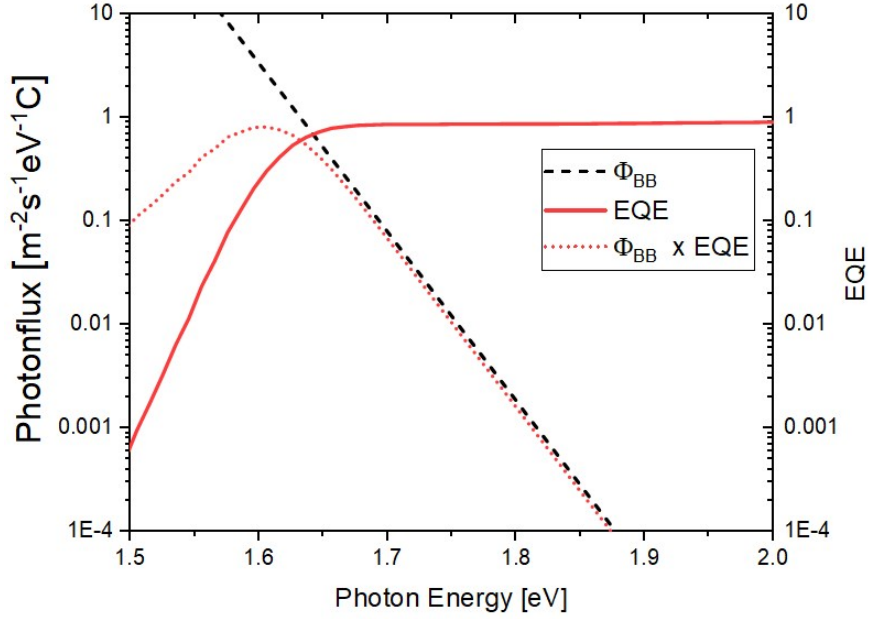


Fig. S13: EQE_{PV} onset of the PIL treated device. The plotted emitted spectral photon flux of the device is calculated when the device is in equilibrium with the black-body (Φ_{BB}) radiation of the surroundings at 300K.

The approach used in Fig. S1 follows the report by Rau et al.¹². Briefly the black body photon flux is

$$\phi_{BB} = \frac{1}{4\pi^2 \hbar^3 c^2} \frac{E^2}{\exp\left(\frac{E}{k_B T}\right) - 1} \quad (S1)$$

with \hbar Planck's constant, k_B Boltzmann constant and T temperature. Assuming that the perovskite solar cell is at 300K in thermal equilibrium with its environment, the dark radiative recombination current is:

$$J_{em,0} = e \int EQE_{PV}(E) \phi_{BB}(E) dE = J_{rad,0} \quad (S2)$$

with EQE_{PV} the photovoltaic *external* quantum efficiency of the perovskite solar cell and $J_{em,0}$ the current giving rise to emission, which also defines the dark radiative recombination current at $V = 0$. From that, the radiative limit of the QFLS ($QFLS_{rad}$) ($EQE_{EL} = 1$) can be calculated with the following equation:

$$QFLS_{rad} = \frac{k_B T}{e} \ln \left(\frac{J_G}{J_{rad,0}} \cdot 1 \right) \quad (S3)$$

where J_G is the generation current under illumination, in this case approximated to the short circuit current J_{sc} . Analogously, the same approach has been applied to the reference sample.

For a more detailed derivation refer to Rau et al.¹²

Moreover, knowing the $Q_{FLS_{rad}}$ and Q_{FLS} in the absorber under 1 sun condition can be calculated by knowing the $PLQY$.

$$Q_{FLS} = k_B T \cdot \ln \left(PLQY \frac{J_G}{J_{o,rad}} \right) = Q_{FLS_{rad}} + k_B T \cdot \ln (PLQY) \quad (S5)$$

S14: Additional Optoelectronic Characterization

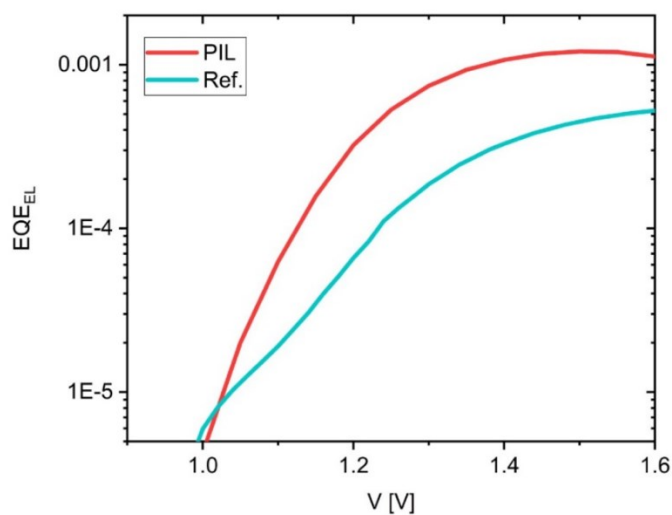


Fig. S14: Electroluminescence quantum yield for reference and PIL treated cells.

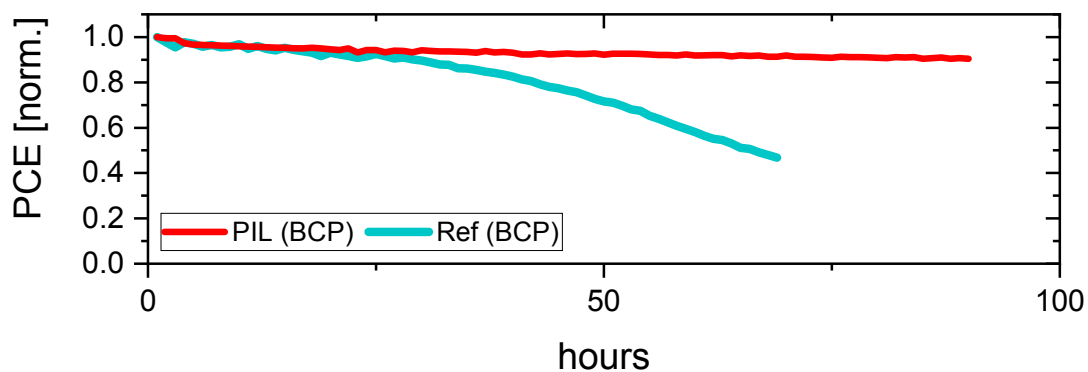


Fig. S15: MPP tracking of a reference sample and PIL treated one at 50°C under N₂ atmosphere under constant illumination at 1 sun equivalent.

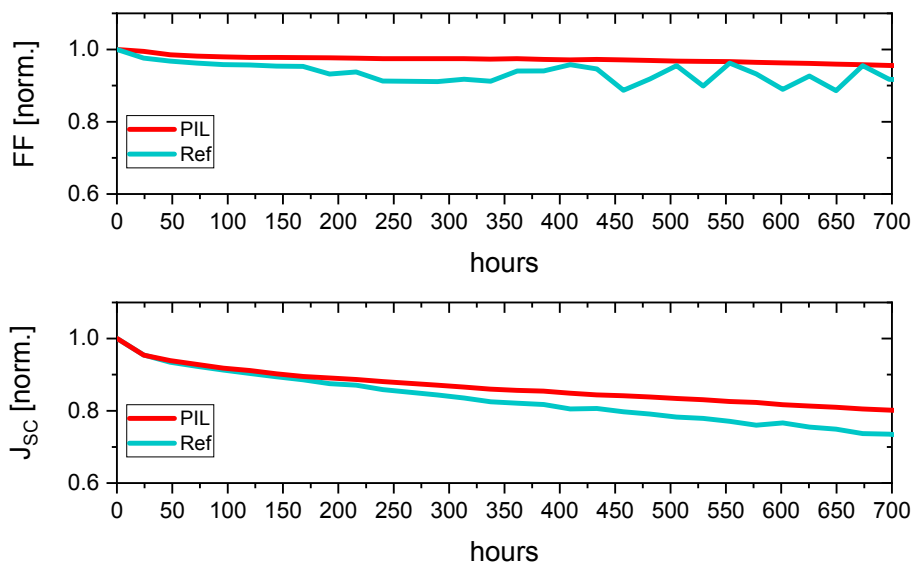


Fig. S16: FF and J_{sc} of the best cells under MPP at 25°C under N_2 atmosphere under constant illumination at 1 sun equivalent over 700h.

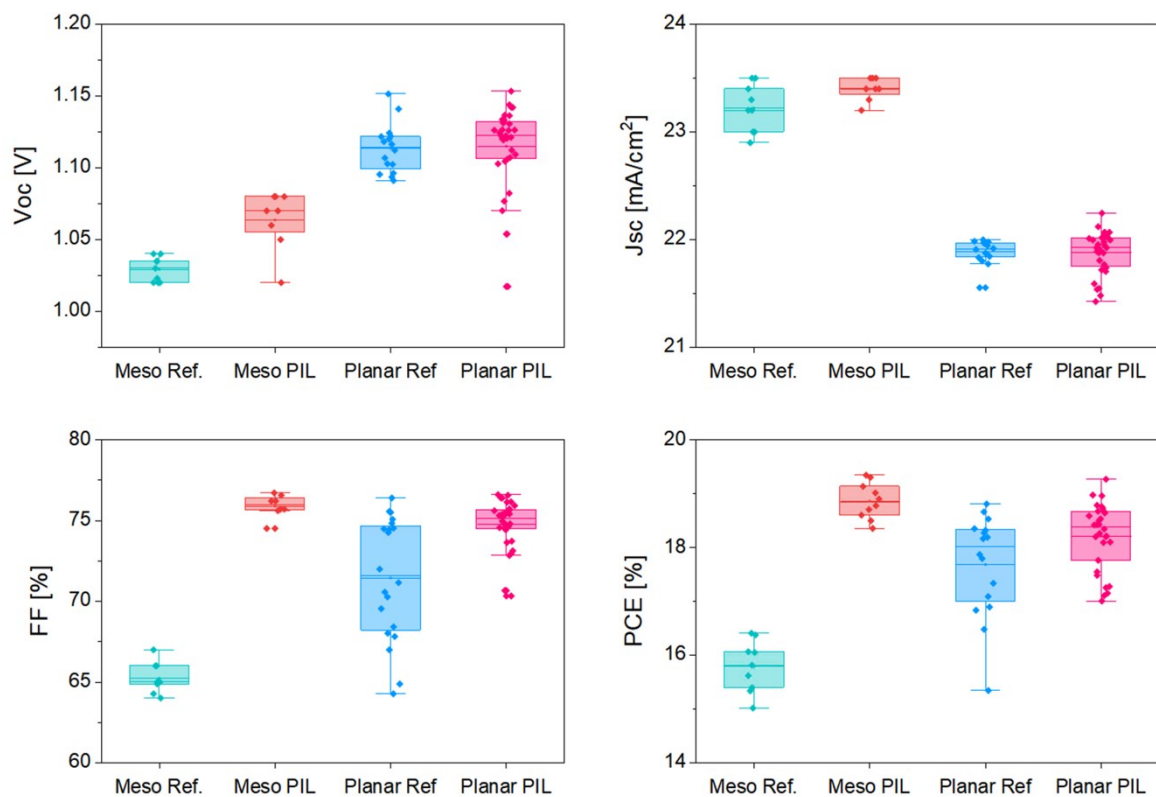


Fig. S17: Statistic of planar SnO_2 and mesoporous TiO_2 nip devices comparing reference cells with PIL treated ones. The interface modified with the PIL is in contact with the doped Spiro in both type of cells.

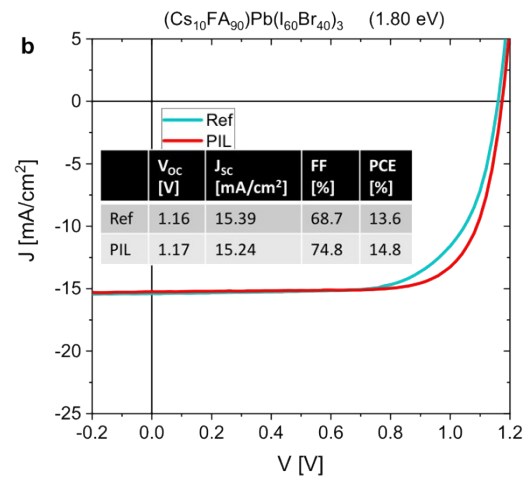
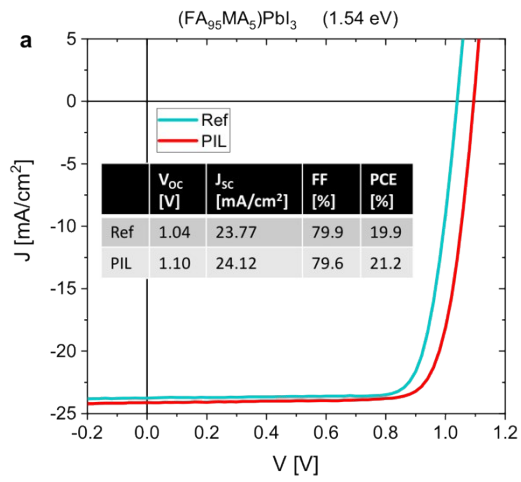


Fig. S18: a) Reference and PIL treated sample for a pin low bandgap perovskite of composition $(FA_{95}MA_5)PbI_3$. b) Reference and PIL treated sample for a pin large bandgap MA-free sample of composition $(Cs_{10}FA_{90})Pb(I_{60}Br_{40})_3$. Both types of devices use PTAA/PFN as HTL and C60 as ETL.

Bibliography

1. Spanos, I. *et al.* Poly(ionic liquid) binders as ionic conductors and polymer electrolyte interfaces for enhanced electrochemical performance of water splitting electrodes. *Sustain. Energy Fuels* **2**, 1446–1451 (2018).
2. Perdew, J. P., Burke, K. & Ernzerhof, M. Generalized gradient approximation made simple. *Phys. Rev. Lett.* **77**, 3865–3868 (1996).
3. Meggiolaro, D. *et al.* Energy Level Tuning at the MAPbI₃ Perovskite/Contact Interface Using Chemical Treatment. *ACS Energy Lett.* **4**, 2181–2184 (2019).
4. Meggiolaro, D. *et al.* Iodine chemistry determines the defect tolerance of lead-halide perovskites. *Energy Environ. Sci.* **11**, 702–713 (2018).
5. Adamo, C. & Barone, V. Toward reliable density functional methods without adjustable parameters: The PBE0 model. *J. Chem. Phys.* **110**, 6158–6170 (1999).
6. Vandevondele, J. *et al.* Quickstep: Fast and accurate density functional calculations using a mixed Gaussian and plane waves approach. *Comput. Phys. Commun.* **167**, 103–128 (2005).
7. Vandevondele, J. & Hutter, J. Gaussian basis sets for accurate calculations on molecular systems in gas and condensed phases. *J. Chem. Phys.* **127**, 114105 (2007).
8. Goedecker, S. & Teter, M. Separable dual-space Gaussian pseudopotentials. *Phys. Rev. B - Condens. Matter Mater. Phys.* **54**, 1703–1710 (1996).
9. Grimme, S., Antony, J., Ehrlich, S. & Krieg, H. A consistent and accurate ab initio parametrization of density functional dispersion correction (DFT-D) for the 94 elements H-Pu. *J. Chem. Phys.* **132**, 154104 (2010).
10. Guidon, M., Hutter, J. & Vandevondele, J. Auxiliary density matrix methods for Hartree-Fock exchange calculations. *J. Chem. Theory Comput.* **6**, 2348–2364 (2010).
11. Stoumpos, C. C., Malliakas, C. D. & Kanatzidis, M. G. Semiconducting tin and lead iodide perovskites with organic cations: Phase transitions, high mobilities, and near-infrared photoluminescent properties. *Inorg. Chem.* **52**, 9019–9038 (2013).
12. Rau, U. Reciprocity relation between photovoltaic quantum efficiency and electroluminescent emission of solar cells. *Phys. Rev. B* **76**, 085303 (2007).